

Signatures of magnetic Weyl fermion annihilation

Ilya Belopolski*,^{1,†} Tyler A. Cochran*,¹ Xiaoxiong Liu*,² Zi-Jia Cheng*,¹ Xian P. Yang,¹ Zurab Guguchia,^{1,3} Stepan S. Tsirkin,² Jia-Xin Yin,¹ Praveen Vir,⁴ Gohil S. Thakur,^{4,5} Songtian S. Zhang,¹ Junyi Zhang,⁶ Konstantine Kaznatcheev,⁷ Guangming Cheng,⁸ Guoqing Chang,⁹ Daniel Multer,¹ Nana Shumiya,¹ Maksim Litskevich,¹ Elio Vescovo,⁷ Timur K. Kim,¹⁰ Cephise Cacho,¹⁰ Nan Yao,⁸ Claudia Felser,⁴ Titus Neupert,² and M. Zahid Hasan^{1,8,11,‡}

¹*Laboratory for Topological Quantum Matter and Spectroscopy (B7),*

*Department of Physics, Princeton University,
Princeton, New Jersey 08544, USA*

²*Department of Physics, University of Zurich,
Winterthurerstrasse 190, 8057 Zurich, Switzerland*

³*Laboratory for Muon Spin Spectroscopy,
Paul Scherrer Institute, Villigen PSI, Switzerland*

⁴*Max Planck Institute for Chemical Physics of Solids,
Nöthnitzer Straße 40, 01187 Dresden, Germany*

⁵*Faculty of Chemistry and Food Chemistry,
Technische Universität, 01069 Dresden, Germany*

⁶*Department of Physics, Princeton University,
Princeton, New Jersey 08544, USA*

⁷*National Synchrotron Light Source II,
Brookhaven National Laboratory, Upton, New York 11973, USA*

⁸*Princeton Institute for Science and Technology of Materials,
Princeton University, Princeton, New Jersey, 08544, USA*

⁹*Division of Physics and Applied Physics,
School of Physical and Mathematical Sciences,
Nanyang Technological University, 21 Nanyang Link, 637371, Singapore*

¹⁰*Diamond Light Source, Didcot OX11 0DE, UK*

¹¹*Materials Sciences Division, Lawrence Berkeley*

* These authors contributed equally to this work.

National Laboratory, Berkeley, CA 94720, USA

(Dated: June 1, 2021)

Abstract

Correlated topological magnets are emerging as a new class of quantum materials, exhibiting exotic interacting fermions and unconventional phase transitions. Despite considerable interest, direct observation of the magnetic manipulation of topological quasiparticles remains limited. Here we report a correlated topological phase transition in a kagome spin-orbit semimetal, examined by high-resolution photoemission spectroscopy. By modulating the magnetic order, we observe a clear exchange gap collapse in our spectra, associated with a large renormalization of a spin-orbit-gapped Weyl loop at the Fermi level. This unexpected response suggests the collapse of opposite-spin partner ferromagnetic Weyl loops into a paramagnetic Dirac loop. Taken together with *ab initio* calculation, our results further indicate that oppositely-charged Weyl points pair up and annihilate under collapse, and the Fermi arc surface states are removed. Our findings suggest a novel topological phase transition driven by magnetic interactions, guiding future exploration of renormalized topology under correlated order parameters.

Quantum magnets exhibiting electronic topology are attracting considerable interest as platforms for correlated topological phases [1–5] and the magnetic manipulation of Weyl and Dirac quasiparticles [6, 7]. To date, spectroscopic signatures of electronic topological ground states have been observed in several magnetic semimetals, comprising magnetic Weyl loops [8]; Weyl points [9–12]; and massive Dirac fermions [13]. In parallel, the magnetic manipulation of Weyl and Dirac fermions has been extensively explored in transport [14–19]. However, direct spectroscopic observation of magnetic control of topology remains challenging. Demonstrating coherent evolution of topological quasiparticles under varying magnetic order, such as the annihilation of Weyl points, offers the possibility to directly verify fundamental notions of topological band theory [2, 3, 20, 21]. At the same time, it is essential to tune the momentum-space separation and distribution of topological objects, control their Fermi velocities, and modulate their relative energies as well as energy offsets from the Fermi level. Such control is a key underlying motivation for the study of magnetic topological quantum matter and should offer new opportunities for well-controlled anomalous transport and optics phenomena, as well as novel responses of renormalized topological states.

We have investigated magnetic modulation of topological semimetallic states in a range of materials by spectroscopy, including Fe_3Sn_2 , Co_2MnGa , PrAlGe , Fe_3GeTe_2 , TbMn_6Sn_6 and $\text{Co}_3\text{Sn}_2\text{S}_2$ [8, 12, 22–24]. Some of these materials exhibit high magnetic transition temperatures > 600 K, so that thermal broadening may fundamentally overwhelm magnetic evolution of the Weyl or Dirac state [8, 13]. Other systems, such as PrAlGe , exhibit low transition temperatures of ~ 10 K, associated with only small magnetic perturbations to the electronic structure [12]. Even in materials such as Fe_3GeTe_2 , with intermediate $T_C = 230$ K, the thermal evolution appears to be dominated by a suppression of quasiparticle lifetime, without significant coherent evolution of the dispersion [25–27]. Using newly available high-quality single crystals combined with state-of-the-art variable-temperature photoemission spectroscopy, we have found that a large and previously overlooked renormalization of a topological Weyl loop occurs in $\text{Co}_3\text{Sn}_2\text{S}_2$ across $T_C = 176$ K [28–32]. This renormalization takes place together with a magnetic exchange gap collapse that suggests a ferromagnetic Weyl to paramagnetic Dirac loop transition on raising temperature. Additionally, our analysis indicates that this transition is accompanied by the removal of candidate topological Fermi arc surface states and the annihilation of Weyl points.

Materials with inversion symmetry, mirror symmetry and ferromagnetism provide a

unique platform for a magnetic-topological phase transition. The ferromagnetism produces singly-degenerate spin-split bands. In the limit of weak spin-orbit coupling (SOC), mirror symmetry can then give rise to Weyl loops on mirror planes of the bulk Brillouin zone [8, 33–35]. A Weyl loop is a closed curve along which the bands are everywhere two-fold degenerate; it is characterized by a π Berry phase topological invariant and a linear energy-momentum dispersion away from the degeneracy loop. If the magnetic order is removed and there is no spin-splitting, the system may instead exhibit a Dirac loop, with four-fold degeneracy along a closed curve in momentum space [35–37]. Weyl loops under finite SOC typically gap out, possibly leaving behind some discrete number of Weyl points. However, due to inversion symmetry, Dirac loops under SOC must gap out fully. Magnetic exchange gap collapse in such a system naturally gives rise to a Weyl to Dirac loop transition in the weak SOC approximation, where two opposite-spin Weyl loops collapse into a single Dirac loop. With SOC taken into account, upon exchange gap collapse the Weyl points must annihilate.

$\text{Co}_3\text{Sn}_2\text{S}_2$ crystallizes in space group $R\bar{3}2/m$ (No. 166), with dihedral point group D_{3d} which includes three mirror planes (Fig. 1a, S3). A scanning tunneling microscopy (STM) topography on the [111] natural cleaving plane, Co/Sn kagome termination, exhibits a weak symmetry-breaking down to three-fold rotation symmetry C_{3z} , consistent with the expected D_{3d} point group (Fig. 1b). Neutron scattering experiments at low temperature show a ferromagnetic order in the material with magnetic moments associated with the Co atoms and oriented along the [111], z direction, with Curie temperature $T_C = 176 \pm 5$ K [38, 39]. Keeping in mind the mirror symmetry and ferromagnetic order, we explore our $\text{Co}_3\text{Sn}_2\text{S}_2$ samples by ARPES at our experimental base temperature, 20 K. Measuring with incident photon energy $h\nu = 130$ eV, on cuts along k_y at fixed $k_x = 0.3 \text{ \AA}^{-1}$ and 1.0 \AA^{-1} , we observe cone-like dispersions straddling the mirror plane M_y (Figs. 1e (i,ii)). Examining next the Fermi surface, we observe point-like electronic structures on M_y (cyan arrows, Fig. 1f; the mirror planes correspond to $\bar{\Gamma} - \bar{M}$). On an energy-momentum spectrum along k_a (symmetry-equivalent to k_x), within the mirror plane, we again observe multiple cone-like dispersions (Fig. 1e (iii)). The observation of multiple cone dispersions along both k_x and k_y , coming together at point Fermi surfaces, suggests a set of band crossings living in the momentum-space mirror plane. To understand the evolution of the band crossings along the third out-of-plane momentum-space direction, k_z we acquire analogous datasets for a wide range of photon energies, from $h\nu = 100$ to 135 eV (Fig. S4). We find that

the cones persist in $h\nu$, with crossing points consistently on the M_y plane, but at varying (k_x, k_z) coordinates (red diamonds, Fig. 1g). Taken together, these crossing points appear to form an extended nodal electronic state encircling the L point of the bulk Brillouin zone, suggesting the observation of a bulk loop node in $\text{Co}_3\text{Sn}_2\text{S}_2$.

Since the system is ferromagnetic with generically singly-degenerate bands, we interpret this loop node as a Weyl loop (Fig. 1d). To provide further evidence for the Weyl loop, we note that certain cones exhibit a hybridization gap of energy scale ~ 10 meV (left-most arrow of Fig. 1e(iii)), consistent with the moderate SOC expected in $\text{Co}_3\text{Sn}_2\text{S}_2$. This signature of an SOC gap provides further evidence for a Weyl loop. To extract the complete trajectory of the loop, it is natural to parametrize its trajectory by an angle ω in polar coordinates with L taken as the origin. The Weyl loop is then described by a function $r(\omega)$ with 2π periodicity. Crystalline inversion symmetry P further requires that the dispersion remain unchanged under inversion through L, constraining the trajectory to $r(\omega + \pi) = r(\omega)$. With π periodicity, the first three terms of the Fourier decomposition are $r(\omega) = r_0 + r_1 \cos(2\omega + \phi_1) + r_2 \cos(4\omega + \phi_2)$. By fitting to the ARPES locations of the cone dispersions, we find that the trajectory of the Weyl loop is given by $r_0 = 0.27 \text{ \AA}^{-1}$, $r_1 = 0.12 \text{ \AA}^{-1}$, $\phi_1 = 43^\circ$, $r_2 = -0.05 \text{ \AA}^{-1}$ and $\phi_2 = 27^\circ$ (blue loop, Fig. 1g). In this way we extract the full momentum-space trajectory of the Weyl loop from photoemission data alone.

Next we explore the evolution of the Weyl loop with temperature. We systematically cycle the temperature of our samples from 20 K to 290 K and back to 20 K, moving across $T_C = 176$ K. We consider Cut (i) through the Weyl loop, at fixed $h\nu = 130$ eV (Fig. 1f). On raising the temperature, we observe a dramatic evolution of the Weyl cone on a large energy scale of ~ 0.1 eV (Fig. 2a), with the cone appearing to recede above E_F . Upon lowering the temperature back down to 20 K, the Weyl cone returns to its initial position, indicating a reversible thermal evolution consistent with a magnetic phase transition. We next assemble the momentum distribution curves (MDCs) of Cut (i) at E_F for all temperatures (Fig. 2b). We find that the temperature dependence of the Weyl loop cone is particularly prominent across T_C , on both the upward and downward sweep, again indicating the magnetic origin of the shift. For further insight, we examine additional spectra on Cut (iv), obtained during the course of the same measurement as Cut (i), and we consider a set of deep bands ~ 0.3 eV below E_F . At 20 K, these deep valence bands exhibit clear splitting, consistent with the material's ferromagnetic order (cyan arrows, Cut (iv), Fig. 2a). Upon raising

the temperature, the splitting appears to vanish and these deep bands collapse together, suggesting a paramagnetic state with spin-degenerate bands (red arrow, Cut (iv)). Upon re-lowering the temperature, these deep bands again split. By examining the evolution of the deep bands, we are able to circumvent the limitations of the photoemission E_F cut-off and observe direct signatures of a prominent magnetic exchange gap collapse across T_C .

To relate the Weyl loop temperature evolution to the magnetic exchange gap collapse, we consider more carefully the interplay between topology and ferromagnetism. In *ab initio* calculation, in the absence of SOC and in the ferromagnetic state, the Weyl loop arises as a crossing of two spin-majority bands, with a spin-minority partner Weyl loop above the Fermi level (schematic blue and green loops, Figs. 2c, S5). In a non-magnetic *ab initio* calculation, the exchange gap vanishes and these two Weyl loops coincide, forming a four-fold degeneracy along a loop—a Dirac loop (purple loop). Comparing the *ab initio* calculations with ARPES, we find that the magnetic Weyl and non-magnetic Dirac nodes exhibit overall agreement with the ferromagnetic and paramagnetic spectra, respectively (Fig. 2c). Note that including SOC in our *ab initio* results does not alter this interpretation, although the expected gap appears in both loop nodes (dashed lines). The agreement between *ab initio* calculations and our ARPES spectra suggests that we have observed the collapse of two opposite-spin ferromagnetic Weyl loops into a paramagnetic Dirac loop across T_C .

To more closely investigate the exchange gap collapse, we extract the band splitting $\Delta(T)$ on an energy distribution curve (EDC) through Cut (iv) (dotted line, Fig. 2d). We compare the resulting $\Delta(T)$ with the magnetization $M(T)$ as measured by a SQUID (Fig. 3a). For $T < T_C$ we find that the exchange splitting tracks $M(T)$. For $T > T_C$ we no longer observe an exchange splitting within our spectral linewidth, consistent with the absence of magnetization by SQUID. The agreement between $\Delta(T)$ and $M(T)$ further suggests the collapse of the exchange gap across T_C in the electronic structure of $\text{Co}_3\text{Sn}_2\text{S}_2$.

To quantitatively characterize the evolution of the Weyl loop under exchange gap collapse, we extract the cone dispersion by fitting a series of Lorentzian peaks to the spectra (Fig. 2e). The extracted dispersions exhibit a clear evolution upward in E_B as the temperature varies from 20 K to 290 K, consistent with an exchange gap collapse. Next we use a linear fit to extract the Fermi velocity $v_F(T)$ of the loop node (Fig. 3b). We find that v_F varies substantially with temperature, from $v_F^{\text{FM}} \sim 0.8 \text{ eV\AA}$ to $v_F^{\text{PM}} \sim 1.3 \text{ eV\AA}$, indicating a renormalization of the Weyl loop by $v_F^{\text{FM}}/v_F^{\text{PM}} \sim 0.6$. The significant reduction of v_F in the

ferromagnetic phase is consistent with the enhancement of electron-electron correlations associated with magnetic order. Moreover, our unscaled *ab initio* calculations exhibit a slight enhancement—not reduction—of v_F in the ferromagnetic state in the bare electronic structure (Fig. 2c), further suggesting that the photoemission spectra reflect correlation-driven renormalization of the loop. Taken together, our analysis suggests a magnetic exchange gap collapse across T_C which drives a Weyl to Dirac loop transition and which is associated with a substantial renormalization of these node loops.

To further explore the paramagnetic Dirac loop we park our apparatus at 220 K, well into the paramagnetic phase, and systematically investigate the electronic structure. At a range of $h\nu$ we observe characteristic point-like iso-energy contours on M_y and related mirror planes (Fig. 4a). Energy-momentum spectra through these point-like contours further exhibit cone-like dispersions straddling M_y (Figs. 4b, S6). The presence of multiple cone dispersions on M_y at a range of $h\nu$ again suggests an extended nodal electronic structure confined to the mirror plane. Since we are in the paramagnetic phase with generically spin-degenerate bands, we interpret these candidate band crossings as four-fold degenerate, forming a Dirac loop. By analogy with our analysis in the ferromagnetic phase, we next systematically collect the locations of all cone dispersions observed in the paramagnetic phase for a wide range of $h\nu$ from 100 to 135 eV (red diamonds, Fig. 4c). We again observe that the cone dispersions appear to encircle the L point of the bulk Brillouin zone. Using a low-order Fourier expansion we experimentally extract the full momentum-space trajectory of the Dirac loop. We also obtained spectra on magnetically-modulated $\text{Ni}_x\text{Co}_{3-x}\text{Sn}_2\text{S}_2$ samples at low temperature, which are consistent with these results (Methods, Figs. S1, S2). A loop node electronic structure persisting into the paramagnetic phase of $\text{Co}_3\text{Sn}_2\text{S}_2$ again suggests the observation of a ferromagnetic Weyl to paramagnetic Dirac loop transition.

Having carefully examined the ferromagnetic Weyl to paramagnetic Dirac loop transition, we now consider our spectra in the spin-orbit coupled (SOC) picture. From symmetry considerations, the Weyl loop generically gaps out under SOC, possibly leaving behind some discrete number of Weyl points. *Ab initio* calculations predict that in $\text{Co}_3\text{Sn}_2\text{S}_2$ each Weyl loop produces two Weyl points above the Fermi level, a result broadly accepted by the community [9–11, 28–32]. Our observation of a Weyl to Dirac loop transition naturally motivates investigation of the Weyl points across T_C . In our non-magnetic *ab initio* calculations under SOC, we observe that pairs of exchange-split Weyl points collapse together and

annihilate, opening a gap of ~ 12 meV. In our photoemission spectra, by comparing the predicted location of the Weyl points above E_F with our experimental Weyl loop trajectory, we find that $h\nu = 120$ eV likely cuts through the ferromagnetic Weyl points. Indeed, at both $T = 20$ K and 220 K, we observe overall agreement between the cone dispersions observed in photoemission and the predicted Weyl points and gapped cone (Figs. 5a,b). To further explore this possible annihilation in our photoemission spectra, we consider the topological Fermi arcs, which can provide signatures of Weyl points living above E_F . In a Fermi surface acquired at 20 K, we observe several sharp arc-shaped states near the expected Weyl points, consistent with topological Fermi arcs in *ab initio* calculation (Figs. 5c, S7). At 220 K all of these surface states vanish, leaving behind only bulk pockets broadly consistent with the low temperature spectra (Fig. 5d). The energy-momentum cuts similarly exhibit a dramatic evolution in which the candidate Fermi arcs disappear on raising the temperature across T_C (Figs. 5e,f). The absence of the candidate Fermi arc states at 220 K provides evidence for the annihilation of Weyl points in the paramagnetic phase.

Our systematic variable-temperature ARPES experiments suggest that pairs of ferromagnetic Weyl loops collapse into paramagnetic Dirac loops across T_C in $\text{Co}_3\text{Sn}_2\text{S}_2$. Taken together with *ab initio* calculations, our results additionally provide evidence for the annihilation of Weyl points concomitant with this collapse, indicating a unique magnetic-topological phase transition in a quantum magnet. Our results pave the way to magnetic design of correlated topological states with exotic transport and optical response.

METHODS

Ni-doped $\text{Co}_3\text{Sn}_2\text{S}_2$: We can more deeply explore the ferromagnetic Weyl to paramagnetic Dirac loop transition in nickel (Ni) doped $\text{Co}_3\text{Sn}_2\text{S}_2$. Our $\text{Ni}_x\text{Co}_{3-x}\text{Sn}_2\text{S}_2$ samples show a well-behaved suppression of ferromagnetism upon increased dopant concentration, with approximately linear decay to zero of the T_C , the magnetization M and the anomalous Hall conductivity σ_{xy}^A as the Ni level varies from $x = 0$ to 0.6 [40]. At the same time, Ni nominally electron dopes the system. This allows photoemission measurements in a reduced-magnetization state with favorable positioning of the Fermi level, while maintaining base temperature for the measurement and consequently providing higher energy resolution. At $x = 0.35$, for $h\nu = 110$ eV, we observe clear point-like Fermi surfaces with sharp cone

dispersion (Figs. S1a,b). This cone dispersion persists for a range of $h\nu$, suggesting that the loop node electronic structure survives in the reduced-magnetization state, again indicating a magnetic Weyl to Dirac loop transition as ferromagnetism is suppressed (Fig. S1c-f).

Summary of Weyl & Dirac loop trajectories: Our results for various nodal loops are summarized in Fig. S2. The momentum-space trajectory of the Ni-doped loop node (green diamonds, Fig. S2) quantitatively agrees with the Weyl and Dirac loop trajectories extracted for the undoped sample. *Ab initio* calculations of the Weyl and Dirac loops in the ferromagnetic and non-magnetic states also broadly agree with the experimentally-observed trajectories, although the loops extracted from photoemission appear somewhat smaller. Our systematic results again suggest a ferromagnetic Weyl to paramagnetic Dirac loop transition.

Single crystal growth: Single crystals of $\text{Co}_3\text{Sn}_2\text{S}_2$ were grown by a self-flux method with the congruent composition. The stoichiometrically-weighted starting materials were put in a graphite crucible sealed in a quartz tube. The samples were heated to 1000°C over 48 hours, left there for 24 hours, and then slowly cooled to 600°C over one week. An annealing process was implemented at 600°C for another 24 hours to produce homogeneous and well-ordered crystals. The compositions and phase structure of the samples were initially checked by energy-dispersive X-ray spectroscopy and powder X-ray diffraction, respectively.

Scanning tunneling microscopy: Single crystals of $\text{Co}_3\text{Sn}_2\text{S}_2$ of size up to $1\text{ mm} \times 1\text{ mm} \times 0.5\text{ mm}$ were cleaved mechanically *in situ* at 77 K in ultra-high vacuum, and then immediately inserted into the STM head, already at the ^4He base temperature, 4.2 K . Topographic images were taken with tunneling junction parameters $V = -100\text{ mV}$, $I = 0.05\text{ nA}$.

Scanning transmission electron microscopy: Thin lamellae for microstructure characterization were prepared from bulk single crystals by focused ion beam cutting using a FEI Helios NanoLab 600 dual beam system (FIB/SEM). Atomic resolution high-angle annular dark-field (HAADF) scanning transmission electron microscopy (STEM) imaging and atomic-level energy-dispersive X-ray spectroscopy (EDS) mapping were performed

on a double Cs-corrected FEI Titan Cubed Themis 300 scanning/transmission electron microscope (S/TEM) equipped with an X-FEG source operated at 300 kV with a Super-X EDS system.

Magnetometry: The magnetization measurement was carried out with a superconducting quantum interference device (SQUID) magnetometer (QuantumDesign) from 2 to 300 K in a magnetic field of 0.01 T applied parallel to the crystallographic c -axis.

Angle-resolved photoemission spectroscopy: Photon-energy-dependent ARPES measurements were carried out at Beamline I05 of Diamond Light Source, Harwell Science Campus, Oxfordshire, UK using a Scienta R4000 electron analyzer with angular resolution $< 0.2^\circ$ and total energy resolution < 13 meV for all photon energies, from 100 to 135 eV, with spot size $50 \mu\text{m} \times 50 \mu\text{m}$ [41]. The sample temperature was 8 K. Temperature-dependent ARPES measurements were carried out at Beamline 5-2 of the Stanford Synchrotron Radiation Lightsource, SLAC in Menlo Park, CA, USA using a Scienta R4000 electron analyzer, with photon energy $h\nu = 130$ eV; angular resolution $< 0.2^\circ$; total energy resolution from 14 meV at 22 K to 30 meV at 280 K; and beam spot size $16 \mu\text{m}$ (vertical) \times $36 \mu\text{m}$ (horizontal). Measurements on $\text{Ni}_x\text{Co}_{3-x}\text{Sn}_2\text{S}_2$ samples were carried out at Beamline 21-ID-1 (ESM-ARPES) of the National Synchrotron Light Source II, BNL in Upton, NY, USA. Samples were cleaved *in situ* and measured under a vacuum of 4×10^{-11} Torr or better for all temperatures. ARPES energy-momentum spectra were low-pass filtered and symmetrized about $k_x = 0 \text{ \AA}^{-1}$. To characterize temperature drift in the experimental apparatus, a full Fermi surface was acquired at each temperature. The temperature drift was found to be $(\delta k_x, \delta k_y) < (\pm 0.02 \text{ \AA}^{-1}, \pm 0.02 \text{ \AA}^{-1})$, comparable to the angular resolution. To extract the dispersions, momentum distribution curves (MDCs) were fit by a sum of two Lorentzians,

$$f(x) = \frac{A_0^2}{(x - B_0)^2 + C_0^2} + \frac{A_1^2}{(x - B_1)^2 + C_1^2}$$

corresponding to the peak of interest and an additional nearby irrelevant peak.

Ab initio calculations: Density functional theory (DFT) calculations with the projected augmented wave (PAW) method were implemented in the Vienna *ab initio* simulation pack-

age (VASP) [42, 43] with generalized gradient approximation (GGA) [44]. For the irreducible Brillouin zone, k -meshes of size $8 \times 8 \times 8$ were used. The spin-orbit coupling energy scale was found to be less than the typical linewidth of the photoemission spectra, so non-relativistic calculations were performed for both the ferromagnetic and non-magnetic states. For comparison with the photoemission spectra, the Fermi level of the *ab initio* calculation was optimized to match the experimental results, giving an effective hole-doping of 0.1 eV for the ferromagnetic state and electron-doping of 0.07 eV for the non-magnetic state, of ARPES relative to DFT. The Sn-terminated surface spectral function calculated by the Wannier-Tools package [45], using a tight-binding model generated from maximally-localized Wannier functions [46].

ACKNOWLEDGMENTS

I.B. acknowledges the generous support of the Special Postdoctoral Researchers Program, RIKEN during the late stages of this work. The authors thank D. Lu and M. Hashimoto at Beamline 5-2 of the Stanford Synchrotron Radiation Lightsource (SSRL) at the SLAC National Accelerator Laboratory, CA, USA for support. The authors thank Diamond Light Source for access to Beamline I05 (SI17924, SI19313). This research used Beamline 21-ID-1 (ESM-ARPES) of the National Synchrotron Light Source II, a U.S. Department of Energy (DOE) Office of Science User Facility operated for the DOE Office of Science by Brookhaven National Laboratory under Contract No. DE-SC0012704. The authors also acknowledge use of Princeton University’s Imaging and Analysis Center, which is partially supported by the Princeton Center for Complex Materials (PCCM), a National Science Foundation (NSF)-MRSEC program (DMR-2011750). Use of the Stanford Synchrotron Radiation Lightsource (SSRL), SLAC National Accelerator Laboratory, is supported by the U.S. Department of Energy, Office of Science, Office of Basic Energy Sciences, under contract no. DE-AC02-76SF00515. T.A.C. acknowledges the support of the National Science Foundation Graduate Research Fellowship Program (DGE-1656466). T.N. and S.S.T. acknowledge support from the European Union Horizon 2020 Research and Innovation Program (ERC-StG-Neupert-757867-PARATOP). S.S.T. and T.N. also acknowledge support from the Swiss National Science Foundation (Grant Number: PP00P2-176877). X.L. acknowledges financial support from the China Scholarship Council. G.C. would like to acknowledge the support of the

National Research Foundation, Singapore under its NRF Fellowship Award (NRF-NRFF13-2021-0010) and the Nanyang Assistant Professorship grant from Nanyang Technological University.

† Electronic address: ilyab@princeton.edu

‡ Electronic address: mzhasan@princeton.edu

- [1] E. H. da Silva Neto, “Weyl”ing away time-reversal symmetry. *Science* **365**, 1248 (2019).
- [2] N. P. Armitage, E. J. Mele, A. Vishwanath, Weyl and Dirac semimetals in three-dimensional solids. *Rev. Mod. Phys.* **90**, 015001 (2018).
- [3] M. Z. Hasan, S.-Y. Xu, I. Belopolski, S.-M. Huang, Discovery of Weyl fermion semimetals and topological Fermi arc states. *Ann. Rev. Cond. Matt. Phys.* **8**, 289 (2017).
- [4] J. Maciejko, G. A. Fiete, Fractionalized topological insulators. *Nat. Phys.* **11**, 385 (2015).
- [5] M. Z. Hasan, *et al.*, Weyl, Dirac and high-fold chiral fermions in topological quantum matter. *Nat. Rev. Mat.* (2021).
- [6] B. Keimer, J. E. Moore, The physics of quantum materials. *Nat. Phys.* **13**, 1045 (2017).
- [7] D. N. Basov, R. D. Averitt, D. Hsieh, Towards properties on demand in quantum materials. *Nat. Mat.* **16**, 1077 (2017).
- [8] I. Belopolski, *et al.*, Discovery of topological Weyl fermion lines and drumhead surface states in a room temperature magnet. *Science* **365**, 1278 (2019).
- [9] E. Liu, *et al.*, Giant anomalous Hall effect in a ferromagnetic kagome-lattice semimetal. *Nat. Phys.* **14**, 1125 (2018).
- [10] N. Morali, *et al.*, Fermi-arc diversity on surface terminations of the magnetic Weyl semimetal $\text{Co}_3\text{Sn}_2\text{S}_2$. *Science* **365**, 1286 (2019).
- [11] D. F. Liu, *et al.*, Magnetic Weyl semimetal phase in a Kagomé crystal. *Science* **365**, 1282 (2019).
- [12] D. S. Sanchez, *et al.*, Observation of Weyl fermions in a magnetic non-centrosymmetric crystal. *Nat. Commun.* **11**, 3356 (2020).
- [13] L. Ye, *et al.*, Massive Dirac fermions in a ferromagnetic kagome metal. *Nature* **555**, 638 (2018).
- [14] J. Hu, S.-Y. Xu, N. Ni, Z. Mao, Transport of topological semimetals. *Ann. Rev. Cond. Mat. Phys.* **49**, 207 (2019).

- [15] J. Xiong, *et al.*, Evidence for the chiral anomaly in the Dirac semimetal Na₃Bi. *Science* **350**, 413 (2015).
- [16] C.-L. Zhang, *et al.*, Magnetic-tunnelling-induced Weyl node annihilation in TaP. *Nat. Phys.* **13**, 979 (2017).
- [17] K. Manna, *et al.*, From Colossal to Zero: Controlling the Anomalous Hall Effect in Magnetic Heusler Compounds via Berry Curvature Design. *Phys. Rev. X* **8**, 041045 (2018).
- [18] A. Sakai, *et al.*, Giant anomalous Nernst effect and quantum-critical scaling in a ferromagnetic semimetal. *Nat. Phys.* **14**, 1119 (2018).
- [19] K. Kuroda, *et al.*, Evidence for magnetic Weyl fermions in a correlated metal. *Nat. Mat.* **16**, 1090 (2017).
- [20] A. A. Burkov, L. Balents, Weyl Semimetal in a Topological Insulator Multilayer. *Phys. Rev. Lett.* **107**, 127205 (2011).
- [21] X. Wan, A. M. Turner, A. Vishwanath, S. Y. Savrasov, Topological semimetal and Fermi-arc surface states in the electronic structure of pyrochlore iridates. *Phys. Rev. B* **83**, 205101 (2011).
- [22] J.-X. Yin, *et al.*, Giant and anisotropic many-body spin-orbit tunability in a strongly correlated kagome magnet. *Nature* (2018).
- [23] J.-X. Yin, *et al.*, Quantum-limit Chern topological magnetism in TbMn₆Sn₆. *Nature* **583**, 533 (2020).
- [24] J.-X. Yin, *et al.*, Negative flat band magnetism in a spin-orbit-coupled correlated kagome magnet. *Nat. Phys.* **15**, 443 (2019).
- [25] K. Kim, *et al.*, Large anomalous Hall current induced by topological nodal lines in a ferromagnetic van der Waals semimetal. *Nat. Mat.* **17**, 794 (2018).
- [26] Y. Zhang, *et al.*, Emergence of Kondo lattice behavior in a van der Waals itinerant ferromagnet, Fe₃GeTe₂. *Sci. Adv.* **4**, eaao6791 (2018).
- [27] X. Xu, *et al.*, Signature for non-Stoner ferromagnetism in the van der Waals ferromagnet Fe₃GeTe₂. *Phys. Rev. B* **101**, 201104 (2020).
- [28] Q. Xu, *et al.*, Topological surface Fermi arcs in the magnetic Weyl semimetal Co₃Sn₂S₂. *Phys. Rev. B* **97**, 235416 (2018).
- [29] Q. Wang, *et al.*, Large intrinsic anomalous Hall effect in half-metallic ferromagnet Co₃Sn₂S₂ with magnetic Weyl fermions. *Nat. Commun.* **9**, 3681 (2018).

- [30] Z. Guguchia, *et al.*, Tunable anomalous Hall conductivity through volume-wise magnetic competition in a topological kagome magnet. *Nat. Commun.* **11**, 559 (2020).
- [31] Y. Okamura, *et al.*, Giant magneto-optical responses in magnetic Weyl semimetal $\text{Co}_3\text{Sn}_2\text{S}_2$. *Nat. Commun.* **11**, 4619 (2020).
- [32] R. Yang, *et al.*, Magnetization-Induced Band Shift in Ferromagnetic Weyl Semimetal $\text{Co}_3\text{Sn}_2\text{S}_2$. *Phys. Rev. Lett.* **124**, 077403 (2020).
- [33] Y. Wang, R. Nandkishore, Topological surface superconductivity in doped Weyl loop materials. *Phys. Rev. B* **95**, 060506 (2017).
- [34] O. Stenull, C. L. Kane, T. C. Lubensky, Topological phonons and Weyl lines in three dimensions. *Phys. Rev. Lett.* **117**, 068001 (2016).
- [35] R. Nandkishore, Weyl and Dirac loop superconductors. *Phys. Rev. B* **93**, 020506(R) (2016).
- [36] Y. Kim, B. J. Wieder, C. L. Kane, A. M. Rappe, Dirac line nodes in inversion-symmetric crystals. *Phys. Rev. Lett.* **115**, 036806 (2015).
- [37] A. Yamakage, Y. Yamakawa, Y. Tanaka, Y. Okamoto, Line-Node Dirac Semimetal and Topological Insulating Phase in Noncentrosymmetric Pnictides CaAgX ($X = \text{P}, \text{As}$). *J. of the Phys. Soc. of Jpn.* **85**, 013708 (2016).
- [38] P. Vaqueiro, G. G. Sobany, A powder neutron diffraction study of the metallic ferromagnet $\text{Co}_3\text{Sn}_2\text{S}_2$. *Solid State Sci.* **11**, 513 (2009).
- [39] W. Schnelle, *et al.*, Ferromagnetic ordering and half-metallic state of $\text{Sn}_2\text{Co}_3\text{S}_2$ with the shandite-type structure. *Phys. Rev. B* **88**, 144404 (2013).
- [40] G. S. Thakur, *et al.*, Intrinsic Anomalous Hall Effect in Ni-Substituted Magnetic Weyl Semimetal $\text{Co}_3\text{Sn}_2\text{S}_2$. *Chem. Mat.* **32**, 1612 (2020).
- [41] M. Hoesch, *et al.*, A facility for the analysis of the electronic structures of solids and their surfaces by synchrotron radiation photoelectron spectroscopy. *Rev. Sci. Inst.* **88**, 013106 (2017).
- [42] G. Kresse, J. Furthmüller, Efficient iterative schemes for *ab initio* total-energy calculations using a plane-wave basis set. *Phys. Rev. B* **54**, 11169 (1996).
- [43] G. Kresse, J. Furthmüller, Efficiency of *ab-initio* total energy calculations for metals and semiconductors using a plane-wave basis set. *Comp. Mat. Sci.* **6**, 15 (1996).
- [44] J. P. Perdew, K. Burke, M. Ernzerhof, Generalized gradient approximation made simple. *Phys. Rev. Lett.* **77**, 3865 (1996).
- [45] Q. S. Wu, S. Zhang, H.-F. Song, M. Troyer, A. A. Soluyanov, WannierTools: an open-source

- software package for novel topological materials. *Comput. Phys. Commun.* **224**, 405 (2018).
- [46] G. Pizzi, *et al.*, Wannier90 as a community code: new features and applications. *J. Phys.: Cond. Mat.* **32**, 165902 (2020).

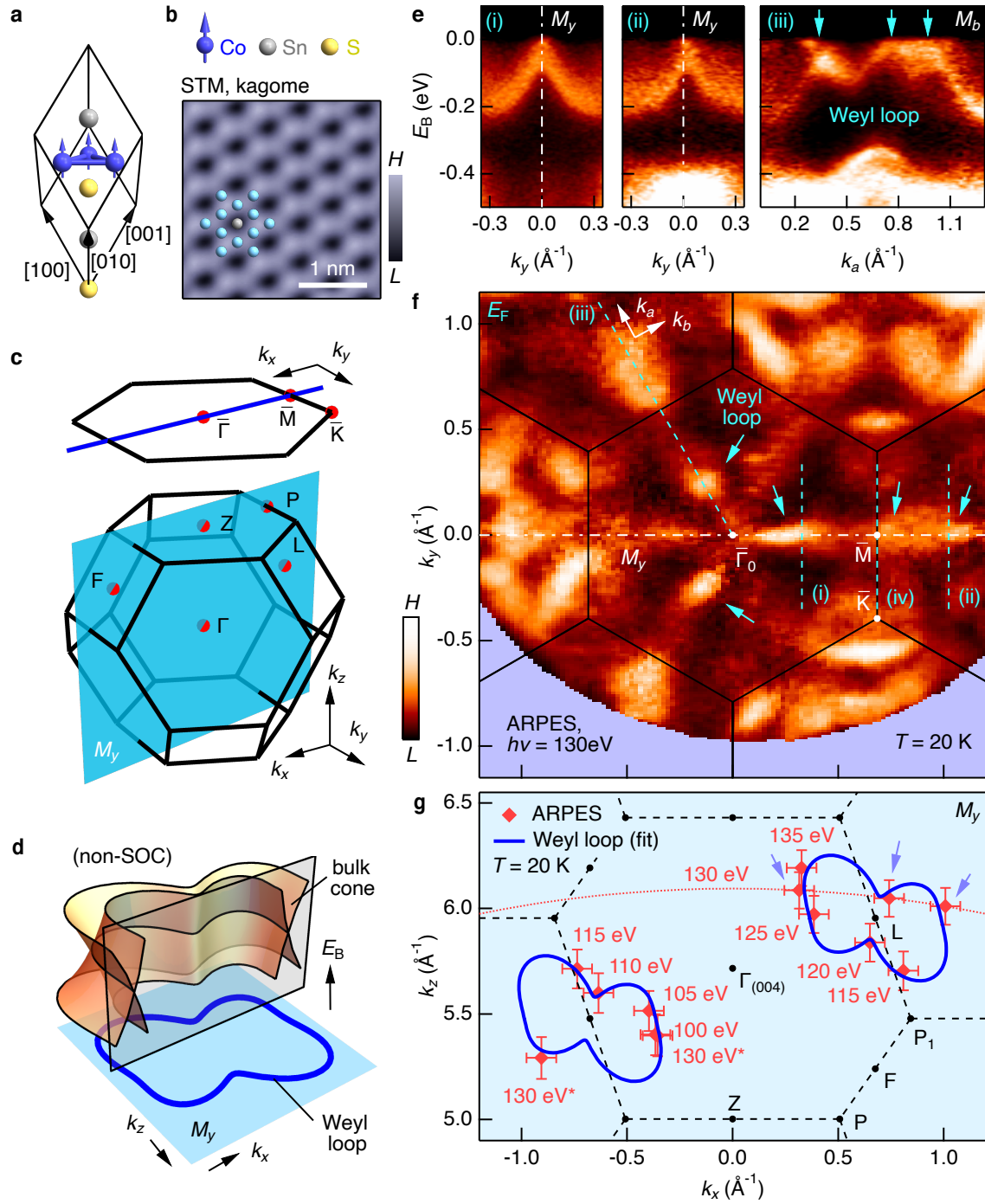


FIG. 1: Topological magnetic Weyl loop. (a) Primitive unit cell of $\text{Co}_3\text{Sn}_2\text{S}_2$, with the crystallographic mirror plane apparent (perpendicular to the page, cutting vertically down the center of the cell). (b) Topograph of the [111] plane, kagome Co/Sn termination, acquired by scanning tunneling microscopy (STM). (c) Bulk and (111) surface Brillouin zones with bulk mirror plane (M_y , cyan), surface mirror line (blue) and several high-symmetry points (red) marked. This surface zone corresponds to the natural cleaving plane. (d) In the absence of spin-orbit coupling (SOC), the combination of mirror symmetry and ferromagnetism generically gives rise to Weyl loops, which live in the mirror planes of the bulk Brillouin zone. A Weyl loop exhibits a ring of band crossings along a closed curve in momentum space (blue loop) with a linear cone dispersion on any energy-momentum slice through the loop. Under SOC, the Weyl loop typically gaps, possibly leaving behind Weyl points. (e) Multiple cone-like dispersions near the Fermi level in energy-momentum ARPES spectra of $\text{Co}_3\text{Sn}_2\text{S}_2$, acquired at $T = 20$ K and photon energy $h\nu = 130$ eV. Spectra (i), (ii): transverse to the mirror plane; spectrum (iii): contained within the mirror plane. (f) ARPES Fermi surface exhibiting multiple dot features (cyan arrows) on the mirror planes (corresponding to $\bar{\Gamma} - \bar{M}$). The dots match up with the cone dispersions in (e). (g) Collecting cone dispersions for a range of $h\nu$ suggests a loop of band crossings (red diamonds) living in M_y and encircling the bulk L point. The crossing points can be fit by a low-order polar coordinate Fourier decomposition around the L point (blue curve, see main text). Different $h\nu$ sample different out-of-plane k_z momenta; representative sample slice shown for 130 eV (dotted red curve).

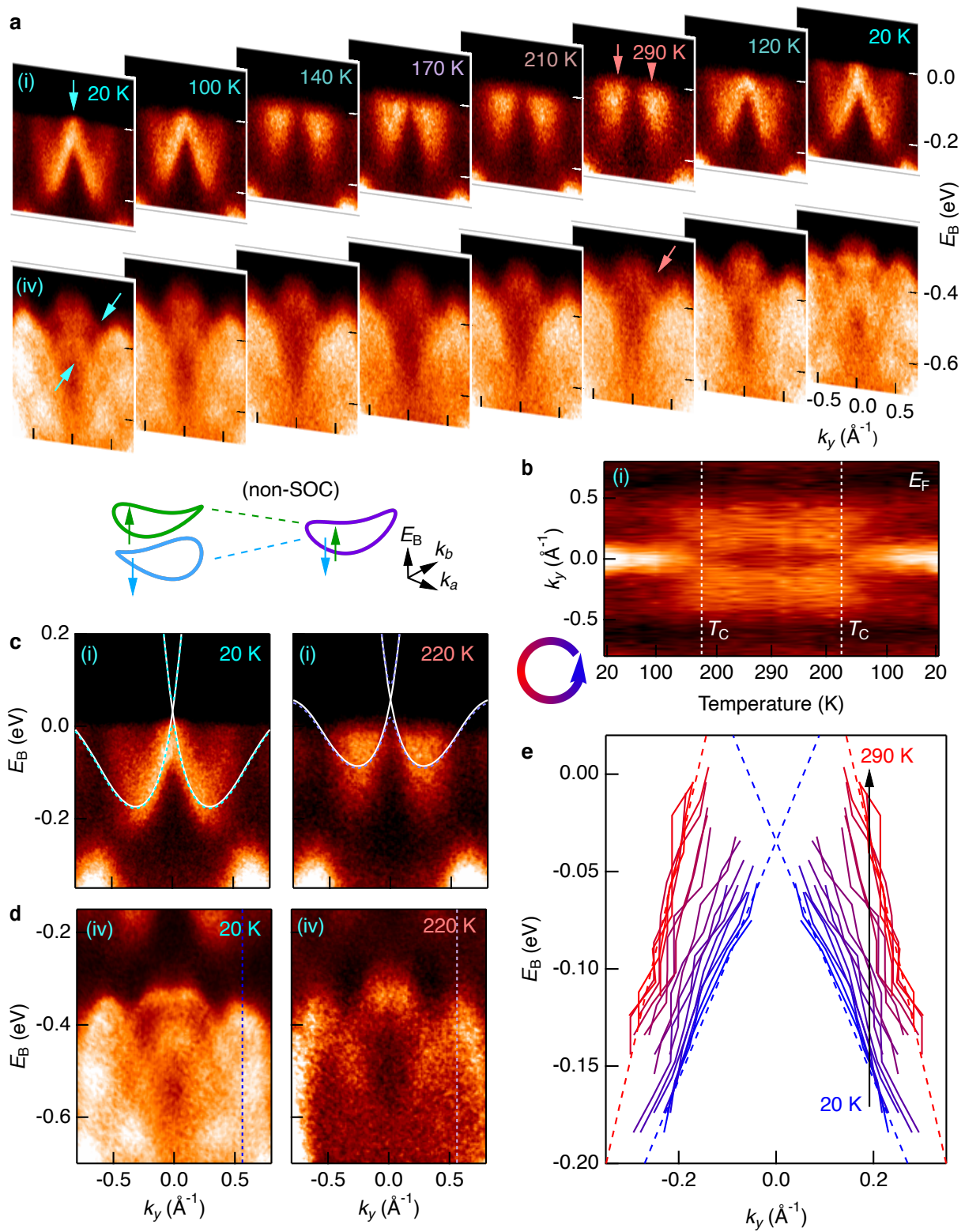


FIG. 2: **Magnetic Weyl to Dirac loop transition in $\text{Co}_3\text{Sn}_2\text{S}_2$.** (a) Energy-momentum spectra at Cut (i), through the Weyl loop, and Cut (iv), along $\bar{M} - \bar{K}$ at deeper binding energy, acquired at different temperatures, from 20 K to 290 K and then back down to 20 K; fixed $h\nu = 130$ eV. Curie temperature: $T_C = 176 \pm 5$ K. The cut locations are also indicated in Fig. 1f. (b) Momentum distribution curves (MDCs) at the Fermi level of Cut (i) for the full temperature cycle, 20 K \rightarrow 290 K \rightarrow 20 K. (c) Cut (i) at 20 K and 220 K, with *ab initio* calculation superimposed. Left: calculation in the ferromagnetic state through the Weyl loop, both without SOC (white trace) and with SOC (blue dashed trace). Right: calculation in the non-magnetic state through the Dirac loop. Cartoon: exchange gap collapse of two opposite-spin Weyl loop partners (blue and green) into a single Dirac loop (purple). (d) Cut (iv), exhibiting clear splittings in deeper energy bands at 20 K (left), which collapse together at 220 K (right). (e) Cone dispersion mapped out by Lorentzian fitting of the spectra for all temperatures from 20 K (blue) \rightarrow 290 K (red).

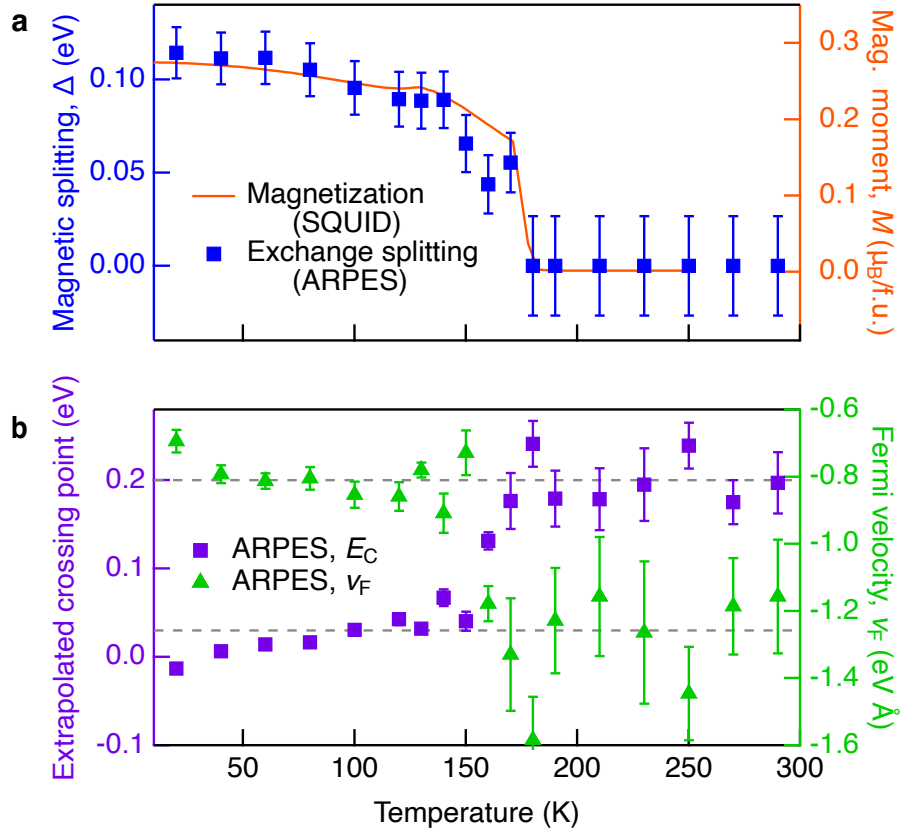


FIG. 3: **Renormalization of a Weyl loop.** (a) Exchange splitting extracted from the temperature dependence on Cut (iv), compared with the magnetization $M(T)$ obtained by a SQUID. (b) Fermi velocity and extrapolated loop node crossing point extracted from linear fits to the dispersions in Fig. 2e.

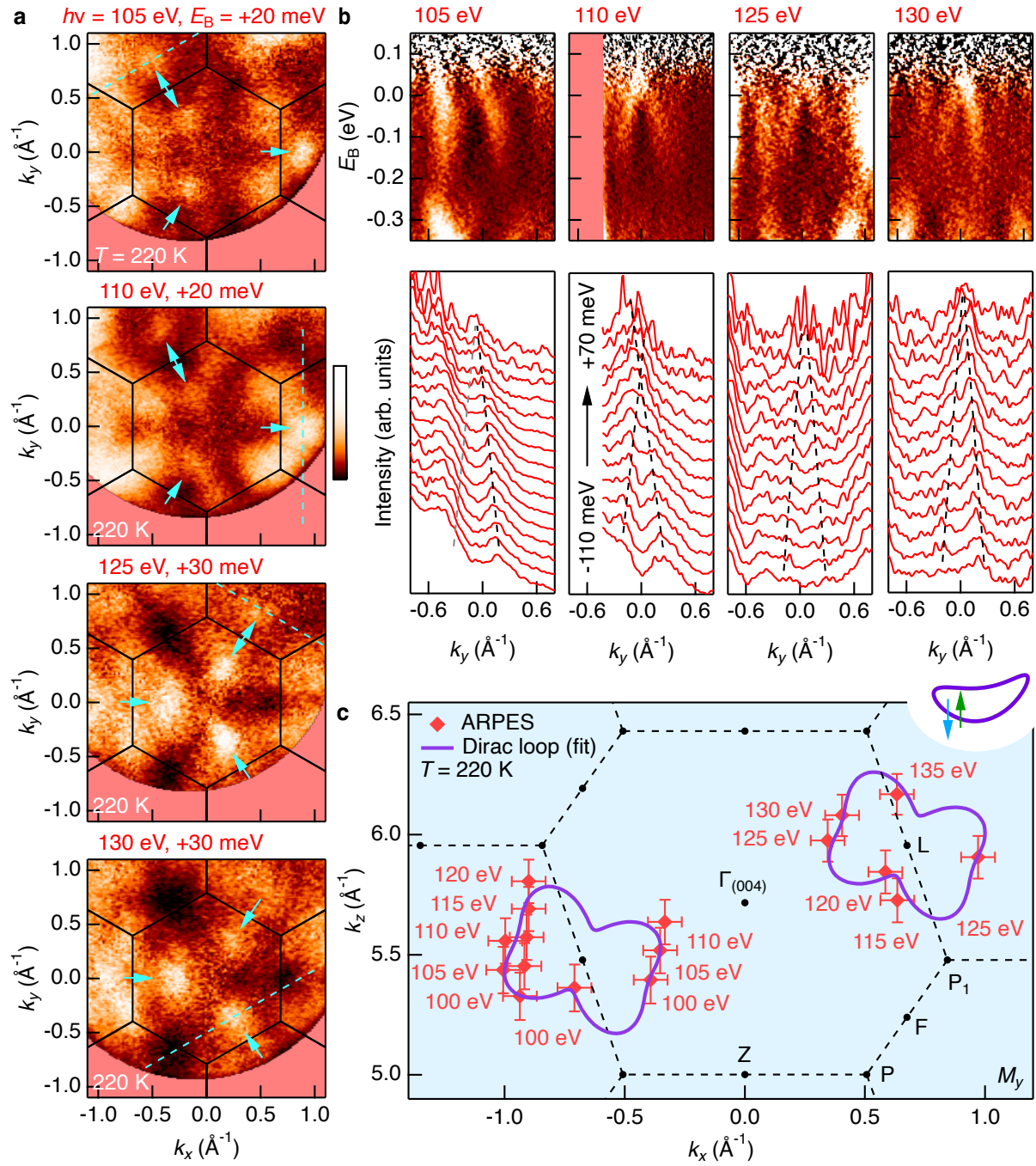


FIG. 4: **Paramagnetic Dirac loop.** (a) ARPES iso-energy contours slightly above E_F , acquired at 220 K, well into the paramagnetic phase on undoped $\text{Co}_3\text{Sn}_2\text{S}_2$. The contours exhibit point-like features (cyan arrows) along $\bar{\Gamma} - \bar{M}$ (corresponding to M_y and the symmetry-related mirror planes). (b) Top: energy-momentum cuts through the point-like features, exhibiting cone dispersions. Each cut location marked on the corresponding iso-energy contour in (a). Bottom: corresponding stack of momentum distribution curves (MDCs) for each cut, with the cone dispersions sketched (dotted black lines). (c) Locations of cones observed for all $h\nu$ (red diamonds). Cones on symmetry-related mirror planes are plotted all together in a single momentum-space mirror plane M_y . The resulting data points are then fit to a low-order polar coordinate Fourier decomposition around the L point (purple curve), mapping out the trajectory of the Dirac loop.

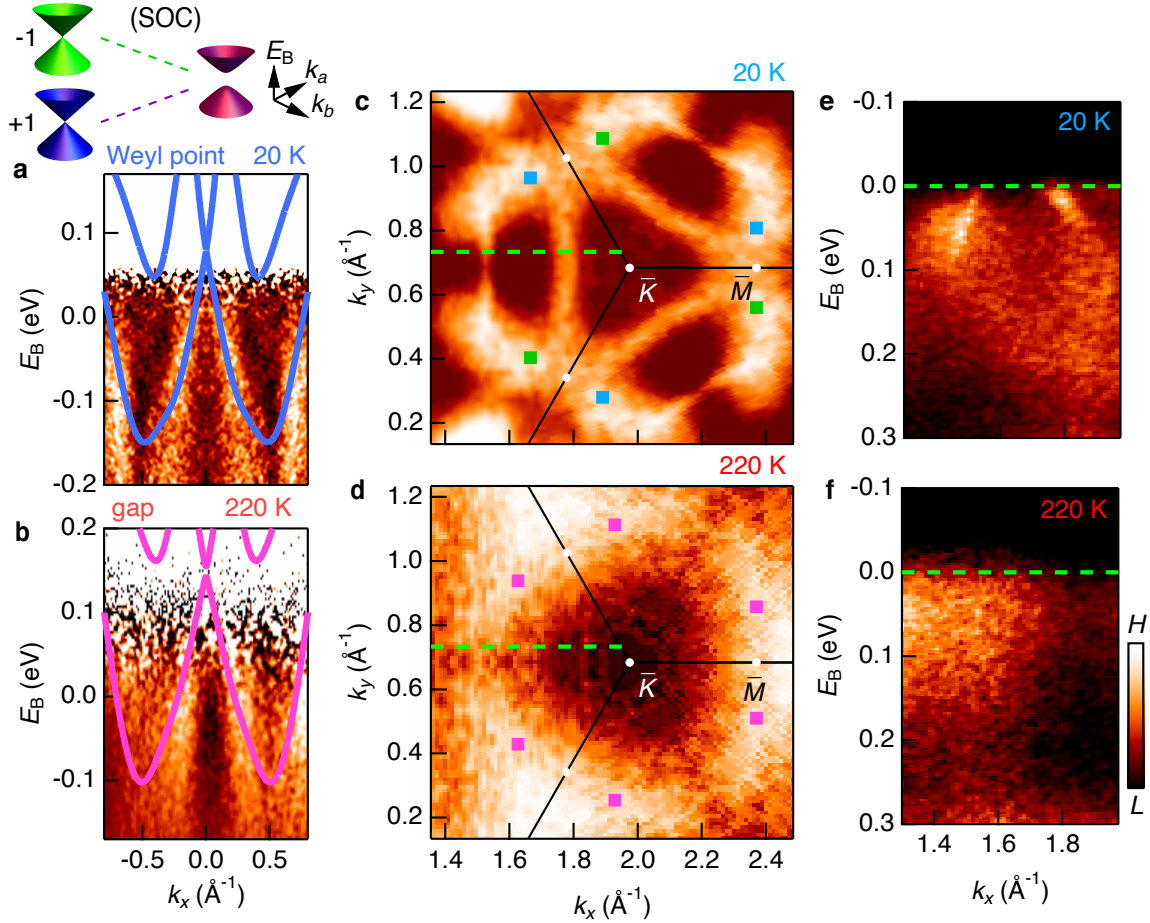


FIG. 5: **Evidence for Weyl point annihilation.** (a) Energy-momentum cut at the location of the Weyl point, as predicted by *ab initio* calculations, in the ferromagnetic phase, $h\nu = 120$ eV. (b) Analogous energy-momentum cut in the paramagnetic phase. The non-magnetic *ab initio* calculation exhibits a gap of ~ 12 meV resulting from annihilation of Weyl points brought together under removal of the exchange gap. *Ab initio* results shifted in energy to match the spectra. Cartoon: collapse of two exchange-split Weyl points (blue and green) and their annihilation (purple). High-temperature spectra acquired under *in situ* potassium K^+ dosing to raise the Fermi level. (c) Fermi surface acquired at $T = 20$ eV, $h\nu = 130$ eV, exhibiting several candidate Fermi arc surface states (sharp branches) near the Weyl point locations, as predicted by *ab initio* calculations (blue, green squares). Data symmetrized for clarity. (d) Analogous Fermi surface at 220 K, exhibiting no surface state features near the annihilation location, as predicted by *ab initio* calculations (magenta squares). (e) Energy-momentum cut through the candidate Fermi arcs at 20 K (green dotted line, (c)). (f) Analogous cut at 220 K, with no signature of Fermi arcs.

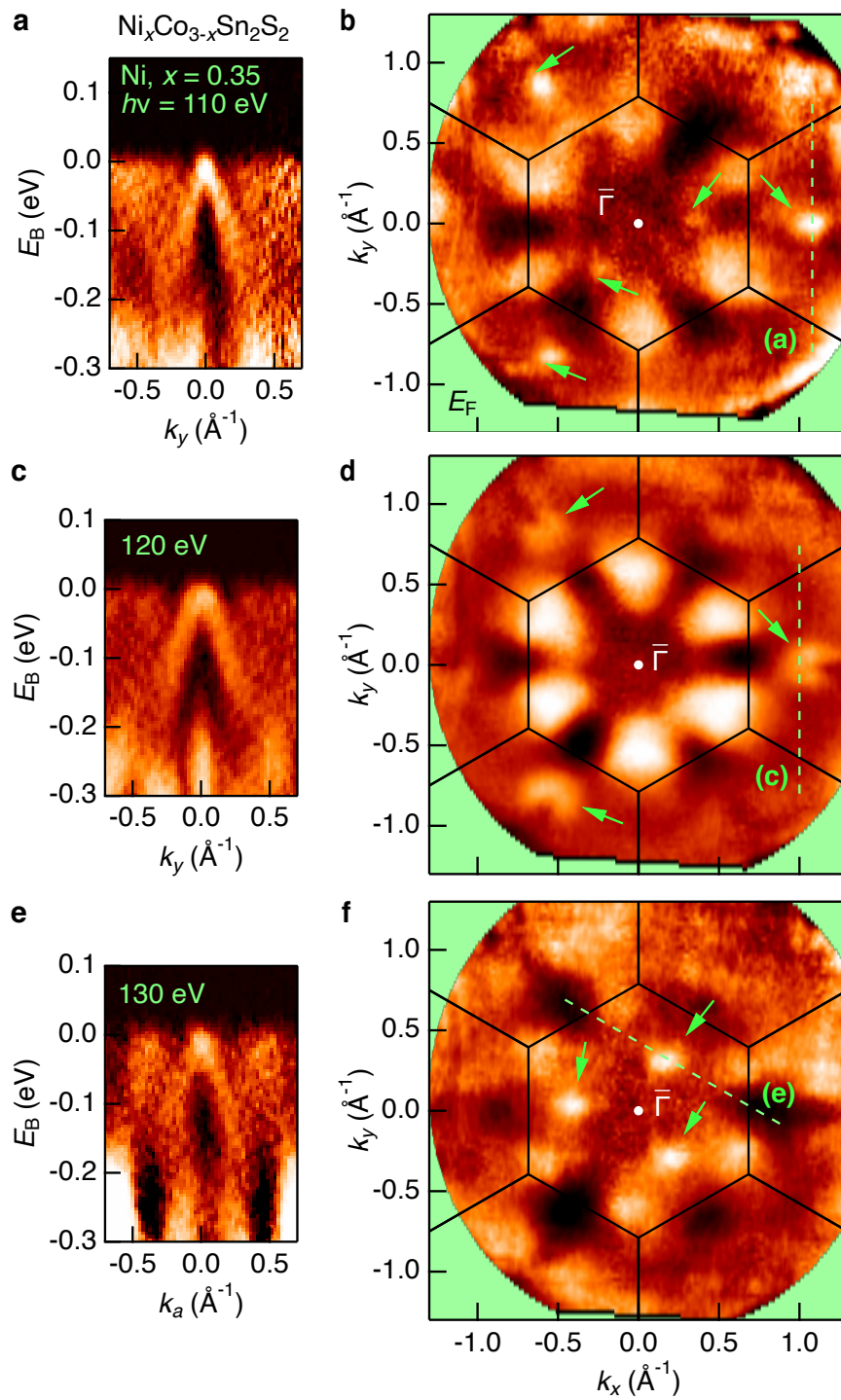


FIG. S1: **Weyl loop, Ni-doped $\text{Co}_3\text{Sn}_2\text{S}_2$.** (a) Energy-momentum ARPES spectrum obtained on ferromagnetically-suppressed $\text{Ni}_x\text{Co}_{3-x}\text{Sn}_2\text{S}_2$ single crystals, $x = 0.35$, at $T = 20$ K and $h\nu = 110$ eV, exhibiting a cone dispersion centered on M_y . (b) Corresponding Fermi surface at 110 eV, exhibiting point-like features (green arrows) on M_y and symmetry-equivalent mirror planes. Spectrum in (d) marked by the dotted green line. (c)-(f) Analogous spectra acquired at $h\nu = 120$ and 130 eV. The energy-momentum spectra again show clear cone dispersions (c, e), corresponding to point-like features (green arrows, d, f) on M_y and equivalent mirror planes.

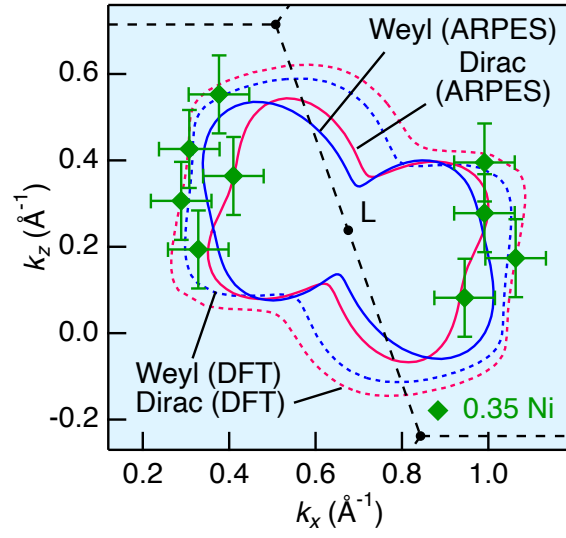


FIG. S2: **Loop node trajectories.** Summary of the ferromagnetic Weyl and paramagnetic Dirac loop trajectories extracted by photoemission; the analogous *ab initio* result in the ferromagnetic and non-magnetic states, in the absence of SOC; and cone dispersions observed in $\text{Ni}_x\text{Co}_{3-x}\text{Sn}_2\text{S}_2$.

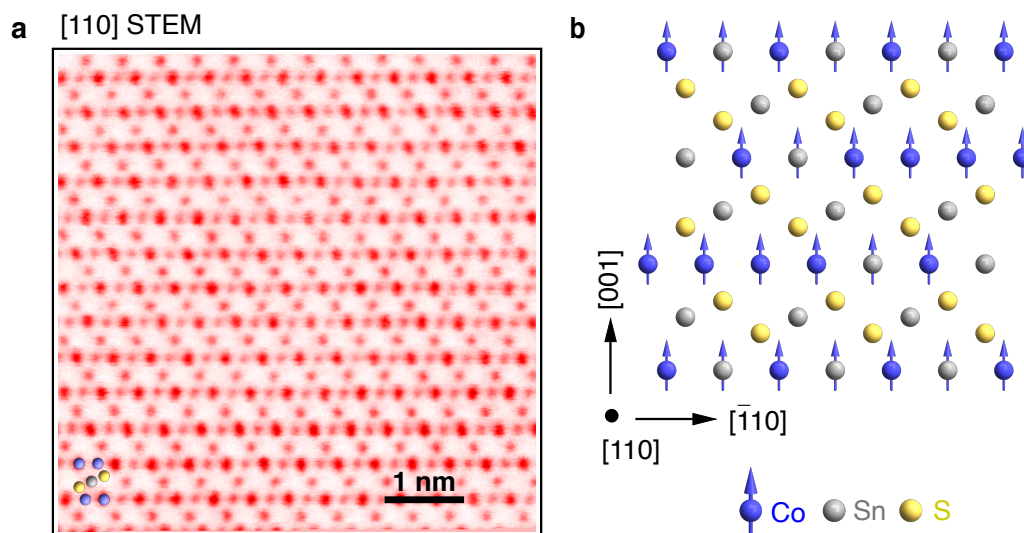


FIG. S3: **Crystal structure.** (a) Crystal structure of $\text{Co}_3\text{Sn}_2\text{S}_2$ along $[110]$, measured by scanning transmission electron microscopy (STEM). (b) Schematic crystal structure viewed along $[110]$, exhibiting the two-fold rotation C_{2x} symmetry.

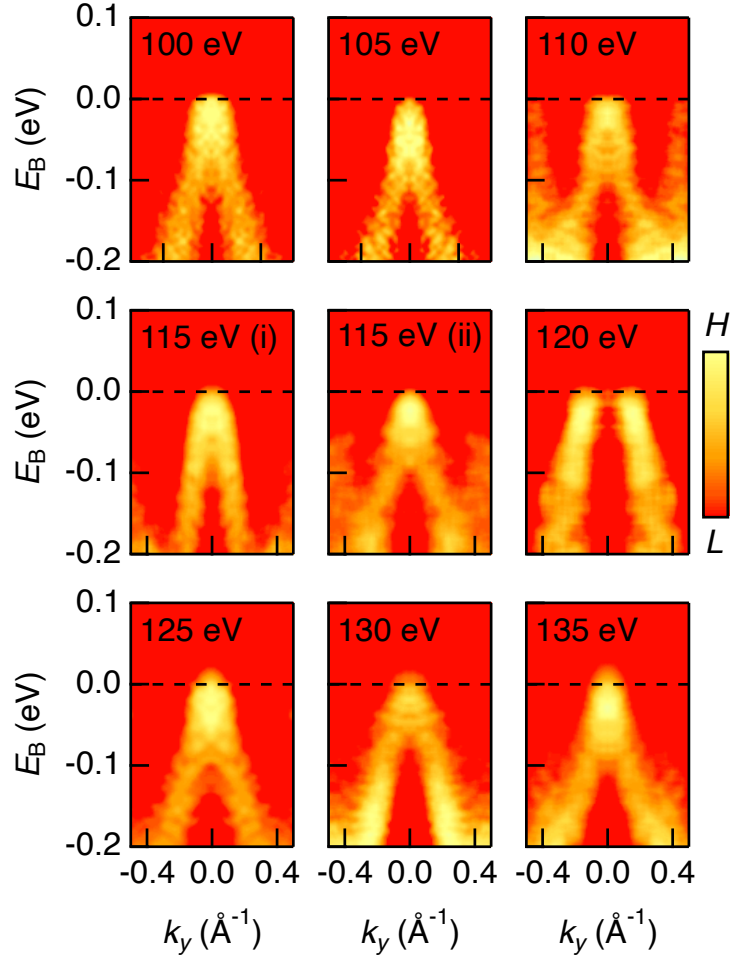


FIG. S4: **Systematics, Weyl loop.** Additional source ARPES energy-momentum spectra used to extract the Weyl loop trajectory in Fig. 1(f), acquired at various $h\nu$ as indicated.

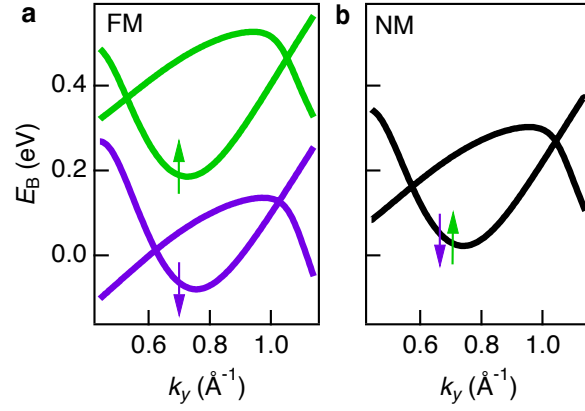


FIG. S5: **Weyl and Dirac loops.** (a) *Ab initio* calculation in the ferromagnetic state, in the absence of SOC. The Weyl loop near E_F is formed from two majority spin bands with a partner Weyl loop of the opposite spin ~ 0.4 eV above E_F . (b) *Ab initio* calculation in the non-magnetic state, in the absence of SOC. The two opposite-spin Weyl loops collapse into a single Dirac loop, characterized by a four-fold band crossing along a loop.

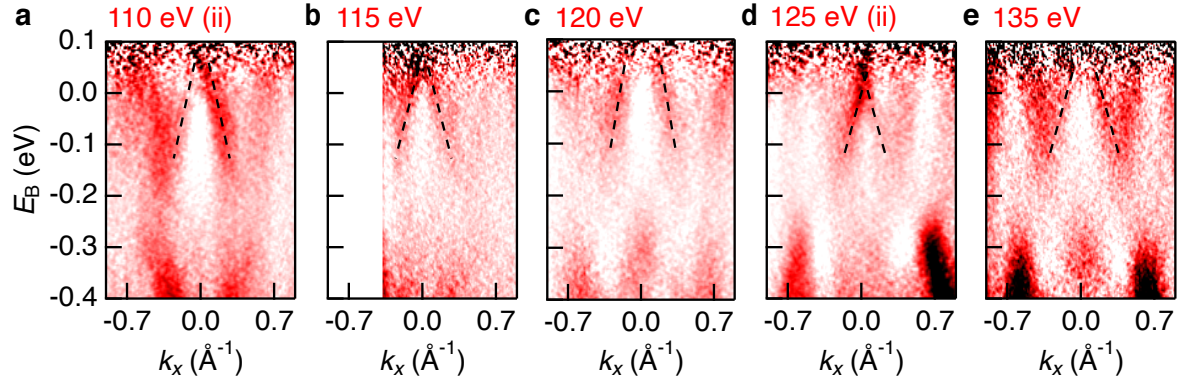


FIG. S6: **Systematics, Dirac loop.** (a)-(e) Additional source ARPES energy-momentum spectra used to extract the Dirac loop trajectory in Fig. 4(c), acquired at various $h\nu$ as indicated. Spectrum (a), 110 eV (ii) was acquired on another, rotated mirror plane relative to the main text 110 eV spectrum, while (d), 125 eV (ii) cuts through the same mirror plane as the main text 125 eV spectrum, but in the first surface Brillouin zone.

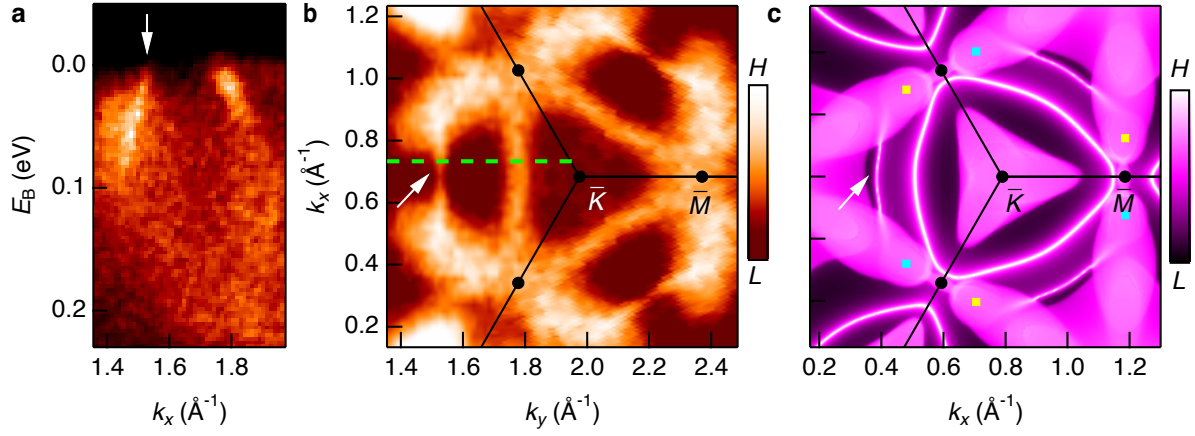


FIG. S7: **Surface state analysis.** (a) Energy-momentum ARPES spectrum and (b) ARPES Fermi surface in the vicinity of the \bar{K} point, acquired at $h\nu = 130$ eV, linear horizontal light polarization, $\bar{\Gamma} - \bar{K}$ APRES slit alignment, second through fourth surface Brillouin zones, $T = 20$ K. White arrows indicate a candidate topological Fermi arc. (c) *Ab initio* calculation of the surface density of states at the Fermi energy, Sn termination, with SOC. Weyl point predictions marked by the yellow (positive chirality) and cyan (negative chirality) squares.